JOURNAL OF SPACECRAFT AND ROCKETS
Vol. 39, No. 4, July–August 2002

Development of a Runge–Kutta Scheme with Total Variation Diminishing for Magnetogasdynamics

Henri-Marie Damevin* and Klaus A. Hoffmann†
Wichita State University, Wichita, Kansas 67260-0044

A four-stage modified Runge–Kutta scheme augmented with the Davis–Yee symmetric total variation diminishing model in a postprocessing stage has been developed to solve the three-dimensional magnetogasdynamic equations. The spatial discretization is performed using finite difference schemes. To be applicable to complex geometries, the system of governing equations and the system eigenstructure have been expressed in a generalized curvilinear coordinate system. The algorithm is validated by solving benchmark problems and is subsequently used in general applications. The shock-capturing properties are demonstrated by simulation of the magnetic shock tube and comparison with solutions computed with other numerical schemes. The implementation of diffusion terms is validated by solving the Hartmann problem, which admits an analytical solution. The performance of the algorithm in multidimensional problems is illustrated in the simulation of ramp flows and convergent channel flows. The method is shown to be accurate, with the ability to capture the physical phenomena arising in magnetogasdynamic flowfields.

Nomenclature

$\boldsymbol{A}$ = convective flux Jacobian matrix in x direction, associated with $\boldsymbol{E}$
B = norm of magnetic field vector, $\|\vec{\boldsymbol{B}}\|$
$\boldsymbol{B}$ = convective flux Jacobian matrix in y direction, associated with $\boldsymbol{F}$
$\vec{\boldsymbol{B}}$ = magnetic field vector

$$\begin{Bmatrix} B_x \\ B_y \\ B_z \end{Bmatrix}$$

$\boldsymbol{C}$ = convective flux Jacobian matrix in z direction, associated with $\boldsymbol{G}$
c_p = specific heat at constant pressure
c_s = speed of sound
$\boldsymbol{D}$ = electric intensity vector
$\boldsymbol{E}$ = convective flux vector in x direction, $\{E\}_{8\times 1}$
$\boldsymbol{E}_v$ = diffusion flux vector in x direction, $\{E_v\}_{8\times 1}$
$\vec{\boldsymbol{E}}$ = electric field
e_t = specific total energy
$\boldsymbol{e}_x, \boldsymbol{e}_y, \boldsymbol{e}_z$ = Cartesian base unit vectors
$\boldsymbol{F}$ = convective flux vector in y direction, $\{F\}_{8\times 1}$
$\boldsymbol{F}_v$ = diffusion flux vector in y direction, $\{F_v\}_{8\times 1}$
$\boldsymbol{f}$ = body force
$\boldsymbol{G}$ = convective flux vector in the z direction, $\{G\}_{8\times 1}$
$\boldsymbol{G}_v$ = diffusion flux vector in the z direction, $\{G_v\}_{8\times 1}$
$\boldsymbol{H}$ = magnetic source flux vector, $\{H\}_{8\times 1}$
$\vec{\boldsymbol{H}}$ = magnetic intensity vector
Ha = Hartmann number
$\bar{\bar{\boldsymbol{I}}}$ = identity tensor
J = Jacobian of transformation
$\boldsymbol{J}$ = current density vector
K = load parameter in Hartmann problem
L = reference length
$\boldsymbol{L}$ = left eigenvector matrix, $\{L\}_{8\times 8}$
M = Mach number
Pr = Prandtl number
p = pressure
$\boldsymbol{Q}$ = solution vector, $\{Q\}_{8\times 1}$
$\boldsymbol{q}$ = surface heat flux
$\boldsymbol{R}$ = right eigenvector matrix, $\{R\}_{8\times 8}$
R_b = magnetic pressure number
Re = Reynolds number
Re_m = magnetic Reynolds number
T = temperature
t = time
U = norm of velocity vector, $\|\boldsymbol{U}\|$
$\boldsymbol{U}$ = velocity vector

$$\begin{Bmatrix} u \\ v \\ w \end{Bmatrix}$$

v_a = speed of Alfvén wave
v_f = speed of fast magnetoacoustic wave
v_s = speed of slow magnetoacoustic wave
x, y, z = Cartesian coordinates
γ = ratio of specific heats
ε_e = electric permittivity
ζ = generalized coordinate
$\zeta_x, \zeta_y, \zeta_z$ = transformation metrics
η = generalized coordinate
η_x, η_y, η_z = transformation metrics
λ = eigenvalue/wave speed
μ = absolute viscosity
μ_e = magnetic permeability
ν_e = magnetic diffusivity ($\nu_e = 1/\mu_e\sigma_e$)
ξ = generalized coordinate
ξ_x, ξ_y, ξ_z = transformation metrics
ρ = density
σ_e = electric conductivity
$\bar{\bar{\tau}}$ = shear stress tensor
$\bar{\boldsymbol{\Phi}}$ = total variation diminishing (TVD) flux limiter function vector, $\{\bar{\Phi}\}_{8\times 1}$
ψ = entropy correction function in TVD scheme

Indices

i = ξ direction
j = η direction
k = ζ direction

Received 8 March 2001; revision received 27 November 2001; accepted for publication 3 December 2001.

*Graduate Research Assistant, Department of Aerospace Engineering. Student Member AIAA.

†Professor, Department of Aerospace Engineering. Associate Fellow AIAA.

Subscripts

a = Alfvén wave
d = magnetic flux wave
e = entropy wave
f = fast magnetoacoustic wave
ref = reference quantity
s = slow magnetoacoustic wave
w = wall quantity
0 = reference quantity or vacuum quantity
∞ = freestream quantity

Superscripts

$*$ = nondimensional quantities
$\bar{}$ = quantity expressed in generalized curvilinear coordinates

Introduction

PHENOMENA associated with the interaction between electrically conducting fluids and magnetic fields are considered in widely diverse fields such as astrophysics, high-temperature physics, nuclear engineering, electrical power generation, etc. In aerospace engineering, the application of magnetogasdynamics (MGD) is investigated for hypersonic flow control. Indeed, at velocity characteristic of spacecraft reentry, thermal ionization enhances the electrical conductivity of the gas in the shock layers, so that it is possible to consider magnetic control for this type of flow. Numerical simulations are essential for understanding these phenomena. Several numerical schemes are available for the solution of one-dimensional MGD equations,[1–6] which have been expressed as either a seven-wave system or an eight-wave system. In 1997, Harada et al.[5] and Augustinus et al.[6] solved one-dimensional ideal MGD equations using a four-stage modified Runge–Kutta (RK4) scheme amended with total variation diminishing (TVD) limiters in a postprocessing stage. Their scheme combined the high-order accuracy and efficiency of the RK4 scheme with the shock-capturing properties of the TVD model. The use of the TVD scheme as a postprocessing technique enhances the performance of the RK4 scheme at relatively low additional computational cost.

The extension of the one-dimensional schemes to multidimensional MGD equations is not straightforward. First, the system of governing equations exhibits a singularity; therefore, a modification has to be introduced,[7] and, second, implementation of several of the numerical schemes requires the determination of the eigenvalues and eigenvectors of the system. Augustinus et al.[8] and Harada et al.[9] developed a two-dimensional version of the RK4 scheme with TVD limiters for the solution of ideal MGD equations. This code has been recently extended to account for gas viscosity and magnetic diffusivity.[10]

MGD effects are three-dimensional. Note that, for two-dimensional flows, the dependent variables (momentum and magnetic fields) are functions of two space variables but possess three components. For simulation of general flowfields, a three-dimensional approach is required. The objectives of the present research activity are to determine the eigenvalues and eigenvectors for the system of three-dimensional MGD equations in generalized coordinates and subsequently develop a modified Runge–Kutta scheme augmented with TVD limiters for three-dimensional applications. The governing equations and the numerical schemes are reviewed in the following sections.

Governing Equations

The governing equations of MGD include equations of electromagnetism and gasdynamics. The electromagnetic constitutive equations for isotropic medium, in the absence of electric polarization and magnetic polarization, are expressed as

$$\boldsymbol{D} = \varepsilon_{e0}\vec{\boldsymbol{E}} \tag{1}$$

$$\vec{\boldsymbol{B}} = \mu_{e0}\vec{\boldsymbol{H}} \tag{2}$$

The pre-Maxwell equations are written as

$$\nabla \cdot \boldsymbol{D} = 0 \tag{3}$$

$$\nabla \cdot \vec{\boldsymbol{B}} = 0 \tag{4}$$

$$\nabla \times \vec{\boldsymbol{H}} = \boldsymbol{J} \tag{5}$$

$$\nabla \times \vec{\boldsymbol{E}} = -\frac{\partial \vec{\boldsymbol{B}}}{\partial t} \tag{6}$$

Equations (3–6) represent, respectively, the Gauss law for electricity in a neutral medium, the Gauss law for magnetism, Ampere's law, and Faraday's law. Ohm's law for isotropic medium, expressed in a reference frame, is assumed to be

$$\boldsymbol{J} = \sigma_e(\vec{\boldsymbol{E}} + \boldsymbol{U} \times \vec{\boldsymbol{B}}) \tag{7}$$

where Hall terms, ions slip, etc. are omitted, which is a reasonable assumption for relatively low magnetic fields. The continuity equation, unaffected by electromagnetism, is

$$\frac{\partial \rho}{\partial t} + \nabla \cdot (\rho \boldsymbol{U}) = 0 \tag{8}$$

The momentum equation for magnetogas is expressed as

$$\frac{\mathrm{D}(\rho \boldsymbol{U})}{\mathrm{D}t} = -\nabla p + \nabla \cdot \bar{\bar{\tau}} + \boldsymbol{J} \times \vec{\boldsymbol{B}} \tag{9}$$

where the $\boldsymbol{J} \times \vec{\boldsymbol{B}}$ term represents the magnetic force. The energy equation is written as

$$\frac{\partial}{\partial t}(\rho e_t) + \nabla \cdot \left[\left(\rho e_t + p + \frac{B^2}{2\mu_{e0}}\right)\boldsymbol{U} - \frac{(\vec{\boldsymbol{B}} \cdot \boldsymbol{U})}{\mu_{e0}}\vec{\boldsymbol{B}}\right]$$
$$= \nabla \cdot (\boldsymbol{U} \cdot \bar{\bar{\tau}}) - \nabla \cdot \boldsymbol{Q} + \frac{J^2}{\sigma_e} \tag{10}$$

where

$$\rho e_t = \rho(U^2/2) + p/(\gamma - 1) + B^2\big/2\mu_{e0} \tag{11}$$

Adequate combinations of the preceding equations lead to a reduction of the number of equations to four main equations (or eight scalar equations in multidimensional case), expressed in terms of four unknowns, namely, ρ, $\rho\boldsymbol{U}$, $\vec{\boldsymbol{B}}$, and ρe_t (or eight scalar unknowns). The interaction of the electromagnetic field on the flowfield is represented by the magnetic field only. The electric field, though present, does not explicitly appear. These equations may be expressed as follows:

$$\frac{\partial}{\partial t}\begin{bmatrix} \rho \\ \rho\boldsymbol{U} \\ \vec{\boldsymbol{B}} \\ \rho e_t \end{bmatrix} + \nabla \cdot \begin{bmatrix} \rho\boldsymbol{U} \\ \rho\boldsymbol{U}\boldsymbol{U} + \left(p + \dfrac{B^2}{2\mu_{e0}}\right)\bar{\bar{\boldsymbol{I}}} - \dfrac{\vec{\boldsymbol{B}}\vec{\boldsymbol{B}}}{\mu_{e0}} \\ \boldsymbol{U}\vec{\boldsymbol{B}} - \vec{\boldsymbol{B}}\boldsymbol{U} \\ \left(\rho e_t + p + \dfrac{B^2}{2\mu_{e0}}\right)\boldsymbol{U} - \dfrac{\vec{\boldsymbol{B}}}{\mu_{e0}}(\boldsymbol{U} \cdot \vec{\boldsymbol{B}}) \end{bmatrix}$$
$$= \begin{bmatrix} 0 \\ \nabla \cdot \bar{\bar{\tau}} \\ \nu_e \nabla^2 \vec{\boldsymbol{B}} \\ \nabla \cdot (\bar{\bar{\tau}} \cdot \boldsymbol{U}) + \nabla \cdot \boldsymbol{q} + \nu_e \dfrac{(\nabla \times \vec{\boldsymbol{B}})^2}{\mu_{e0}} \end{bmatrix} \tag{12}$$

Note, in the subsequent sections, the Joule heating term is omitted, for the sake of simplicity. This assumption has no considerable impact on the solution of ideal MGD flow (because the fluid is infinitely conducting) or incompressible flow (because the energy equation is decoupled).

Cartesian Coordinates

Equation (12) is rearranged in a compact flux vector formulation in Cartesian coordinates as follows:

$$\frac{\partial \boldsymbol{Q}}{\partial t}+\frac{\partial \boldsymbol{E}}{\partial x}+\frac{\partial \boldsymbol{F}}{\partial y}+\frac{\partial \boldsymbol{G}}{\partial z}=\frac{\partial \boldsymbol{E}_v}{\partial x}+\frac{\partial \boldsymbol{F}_v}{\partial y}+\frac{\partial \boldsymbol{G}_v}{\partial z} \tag{13}$$

where

$$\boldsymbol{Q}=\lfloor \rho \quad \rho u \quad \rho v \quad \rho w \quad B_x \quad B_y \quad B_z \quad \rho e_t \rfloor^T \tag{14a}$$

$$\rho e_t=\frac{1}{2}\rho(u^2+v^2+w^2)+\frac{p}{\gamma-1}+\frac{B_x^2+B_y^2+B_z^2}{2\mu_{e0}} \tag{14b}$$

$$\boldsymbol{E}=\left\{\begin{array}{c} \rho u \\ \rho u^2+p+\dfrac{-B_x^2+B_y^2+B_z^2}{2\mu_{e0}} \\ \rho uv-\dfrac{B_xB_y}{\mu_{e0}} \\ \rho uw-\dfrac{B_xB_z}{\mu_{e0}} \\ uB_x-uB_x \\ uB_y-vB_x \\ uB_z-wB_x \\ \left(\rho e_t+p+\dfrac{B_x^2+B_y^2+B_z^2}{2\mu_{e0}}\right)u-\dfrac{B_x}{\mu_{e0}}(uB_x+vB_y+wB_z) \end{array}\right\} \tag{14c}$$

$$\boldsymbol{F}=\left\{\begin{array}{c} \rho v \\ \rho uv-\dfrac{B_xB_y}{\mu_{e0}} \\ \rho v^2+p+\dfrac{B_x^2-B_y^2+B_z^2}{2\mu_{e0}} \\ \rho vw-\dfrac{B_yB_z}{\mu_{e0}} \\ vB_x-uB_y \\ vB_y-vB_y \\ vB_z-wB_y \\ \left(\rho e_t+p+\dfrac{B_x^2+B_y^2+B_z^2}{2\mu_{e0}}\right)v-\dfrac{B_y}{\mu_{e0}}(uB_x+vB_y+wB_z) \end{array}\right\} \tag{14d}$$

$$\boldsymbol{G}=\left\{\begin{array}{c} \rho w \\ \rho uw-\dfrac{B_xB_z}{\mu_{e0}} \\ \rho vw-\dfrac{B_yB_z}{\mu_{e0}} \\ \rho w^2+p+\dfrac{B_x^2+B_y^2-B_z^2}{2\mu_{e0}} \\ wB_x-uB_z \\ wB_y-vB_z \\ wB_z-wB_z \\ \left(\rho e_t+p+\dfrac{B_x^2+B_y^2+B_z^2}{2\mu_{e0}}\right)w-\dfrac{B_z}{\mu_{e0}}(uB_x+vB_y+wB_z) \end{array}\right\} \tag{14e}$$

$$\boldsymbol{E}_v=\left\{\begin{array}{c} 0 \\ \tau_{xx} \\ \tau_{xy} \\ \tau_{xz} \\ \dfrac{1}{\mu_{e0}\sigma_e}\dfrac{\partial B_x}{\partial x} \\ \dfrac{1}{\mu_{e0}\sigma_e}\dfrac{\partial B_y}{\partial x} \\ \dfrac{1}{\mu_{e0}\sigma_e}\dfrac{\partial B_z}{\partial x} \\ u\tau_{xx}+v\tau_{xy}+w\tau_{xz}+q_x \end{array}\right\} \tag{14f}$$

$$\boldsymbol{F}_v=\left\{\begin{array}{c} 0 \\ \tau_{yx} \\ \tau_{yy} \\ \tau_{yz} \\ \dfrac{1}{\mu_{e0}\sigma_e}\dfrac{\partial B_x}{\partial y} \\ \dfrac{1}{\mu_{e0}\sigma_e}\dfrac{\partial B_y}{\partial y} \\ \dfrac{1}{\mu_{e0}\sigma_e}\dfrac{\partial B_z}{\partial y} \\ u\tau_{yx}+v\tau_{yy}+w\tau_{yz}+q_y \end{array}\right\} \tag{14g}$$

$$\boldsymbol{G}_v=\left\{\begin{array}{c} 0 \\ \tau_{zx} \\ \tau_{zy} \\ \tau_{zz} \\ \dfrac{1}{\mu_{e0}\sigma_e}\dfrac{\partial B_x}{\partial z} \\ \dfrac{1}{\mu_{e0}\sigma_e}\dfrac{\partial B_y}{\partial z} \\ \dfrac{1}{\mu_{e0}\sigma_e}\dfrac{\partial B_z}{\partial z} \\ u\tau_{zx}+v\tau_{zy}+w\tau_{zz}+q_z \end{array}\right\} \tag{14h}$$

Enforcement of Gauss Law for Magnetism

In the system of governing equations presented, Eq. (4) is implicitly incorporated, but it is not set as an equation to be solved explicitly. Thus, spurious magnetic field divergence can arise from discretization errors and significantly degrade the solution. Equation (4) causes a fundamental difference between one-dimensional problems and multidimensional problems. In one-dimensional problem, for instance, along the x axis, the solution vector $\boldsymbol{Q}$ has eight components as expressed by Eq. (14a), and Eq. (4) reduces to

$$\frac{\partial B_x}{\partial x}=0 \Rightarrow B_x=\text{const}$$

The constancy of B_x must be met as an initial condition. No evolution equation for B_x requires to be solved. Seven of the eight variables only need to be updated. Therefore, the fifth component of equation is dropped, leading to a seven-wave system. The seven waves, whose speeds constitute the eigenvalues of the system, are one entropy wave traveling with speed $\lambda_e=u$, two Alfvénic waves traveling with the speed $\lambda_a=u\pm v_a$, and two fast and two slow magnetoacoustic waves traveling with the speeds $\lambda_f=u\pm v_f$ and $\lambda_s=u\pm v_s$, respectively. In more than one dimension, Eq. (4) does not lead to the system reduction as noted earlier, that is, the eight-equation structure is required. Linearization of the convective fluxes in Eq. (13), which are not homogeneous of degree one with respect to $\boldsymbol{Q}$, yields

$$\frac{\partial \boldsymbol{Q}}{\partial t} + \boldsymbol{A}\frac{\partial \boldsymbol{Q}}{\partial x} + \boldsymbol{B}\frac{\partial \boldsymbol{Q}}{\partial y} + \boldsymbol{C}\frac{\partial \boldsymbol{Q}}{\partial z} = \frac{\partial \boldsymbol{E}_v}{\partial x} + \frac{\partial \boldsymbol{F}_v}{\partial y} + \frac{\partial \boldsymbol{G}_v}{\partial z} \tag{15}$$

where

$$\boldsymbol{A} = \frac{\partial \boldsymbol{E}}{\partial \boldsymbol{Q}} \tag{16a}$$

$$\boldsymbol{B} = \frac{\partial \boldsymbol{F}}{\partial \boldsymbol{Q}} \tag{16b}$$

$$\boldsymbol{C} = \frac{\partial \boldsymbol{G}}{\partial \boldsymbol{Q}} \tag{16c}$$

It can be shown that the Jacobian matrices $\boldsymbol{A}$, $\boldsymbol{B}$, and $\boldsymbol{C}$ are singular due to the existence of zero eigenvalues. On the one hand, a zero eigenvalue has no physical meaning. As observed in the case of the seven-wave model, the eigenvalues of $\boldsymbol{A}$ should appear either singly as the x component of the flow velocity u, or in pairs symmetric about u. On the other hand, a zero eigenvalue is numerically not desirable because the mode associated with it is undamped. In addition, the existence of zero eigenvalue causes mathematical difficulties in the determination of eigenvectors. To remove the singularity, the methodology introduced by Powell,[7] is extended to the three-dimensional case. For instance, the Jacobian matrices $\boldsymbol{A}$ is modified to meet the following criteria (the same reasoning applied to $\boldsymbol{B}$ and $\boldsymbol{C}$): 1) The eigenvalues and eigenvectors corresponding to the seven-wave mode remain the same. 2) The eigenvalue for the new eighth wave is set equal to u (the only physical choice for a single eigenvalue). 3) The eight-wave model reduces to the seven-wave model in the case $B_x = \text{const}$. The eight waves (in the x direction) are one entropy wave traveling with speed $\lambda_e = u$, two Alfvénic waves traveling with the speed $\lambda_a = u \pm v_a$, two fast and two slow magnetoacoustic waves traveling with the speed $\lambda_f = u \pm v_f$ and $\lambda_s = u \pm v_s$, respectively, and one magnetic flux wave traveling with speed $\lambda_d = u$. The modifications introduced to the Jacobian matrices $\boldsymbol{A}$, $\boldsymbol{B}$, and $\boldsymbol{C}$ lead to an additional terms to the conservative form of the governing equation as

$$\frac{\partial}{\partial t}\begin{bmatrix} \rho \\ \rho \boldsymbol{U} \\ \vec{\boldsymbol{B}} \\ \rho e_t \end{bmatrix} + \nabla \cdot \begin{bmatrix} \rho \boldsymbol{U} \\ \rho \boldsymbol{U}\boldsymbol{U} + \left(p + \dfrac{B^2}{2\mu_{e0}}\right)\bar{\bar{\boldsymbol{I}}} - \dfrac{\vec{\boldsymbol{B}}\vec{\boldsymbol{B}}}{\mu_{e0}} \\ \boldsymbol{U}\vec{\boldsymbol{B}} - \vec{\boldsymbol{B}}\boldsymbol{U} \\ \left(\rho e_t + p + \dfrac{B^2}{2\mu_{e0}}\right)\boldsymbol{U} - \dfrac{\vec{\boldsymbol{B}}}{\mu_{e0}}(\boldsymbol{U}\cdot\vec{\boldsymbol{B}}) \end{bmatrix}$$

$$+ \underbrace{\begin{bmatrix} 0 \\ \dfrac{\vec{\boldsymbol{B}}}{\mu_{e0}} \\ \boldsymbol{U} \\ \boldsymbol{U}\cdot\dfrac{\vec{\boldsymbol{B}}}{\mu_{e0}} \end{bmatrix}}_{\text{additional terms}} \nabla \cdot \vec{\boldsymbol{B}} = \begin{bmatrix} 0 \\ \nabla \cdot \bar{\bar{\tau}} \\ \nu_e \nabla^2 \vec{\boldsymbol{B}} \\ \nabla \cdot (\nabla \cdot \bar{\bar{\tau}}) - \nabla \cdot \boldsymbol{Q} \end{bmatrix} \tag{17}$$

Now Eq. (13), with the additional term $\boldsymbol{H}$, is written as follows:

$$\frac{\partial \boldsymbol{Q}}{\partial t} + \frac{\partial \boldsymbol{E}}{\partial x} + \frac{\partial \boldsymbol{F}}{\partial y} + \frac{\partial \boldsymbol{G}}{\partial z} + \boldsymbol{H} = \frac{\partial \boldsymbol{E}_v}{\partial x} + \frac{\partial \boldsymbol{F}_v}{\partial y} + \frac{\partial \boldsymbol{G}_v}{\partial z} \tag{18}$$

where

$$\boldsymbol{H} = \boldsymbol{H}_M\left(\frac{\partial B_x}{\partial x} + \frac{\partial B_y}{\partial y} + \frac{\partial B_z}{\partial z}\right) \tag{19a}$$

$$\boldsymbol{H}_M = \begin{bmatrix} 0 \\ \dfrac{B_x}{\mu_{e0}} \\ \dfrac{B_y}{\mu_{e0}} \\ \dfrac{B_z}{\mu_{e0}} \\ u \\ v \\ w \\ \dfrac{uB_x + vB_y + wB_z}{\mu_{e0}} \end{bmatrix} \tag{19b}$$

Nondimensional MGD Equations in Generalized Coordinates

To achieve dynamic and energetic similarity between geometrically similar flowfields, Eq. (18) is nondimensionalized using the following variables:

$$(x^*, y^*, z^*) = (x, y, z)/L_{\text{ref}}, \qquad t^* = U_{\text{ref}}t/L_{\text{ref}}, \qquad \rho^* = \rho/\rho_{\text{ref}}$$

$$p^* = p\big/\rho_{\text{ref}}U_{\text{ref}}^2, \qquad T^* = T/T_{\text{ref}}$$

$$(u^*, v^*, w^*) = (u, v, w)/U_{\text{ref}}$$

$$\left(B_x^*, B_y^*, B_z^*\right) = (B_x, B_y, B_z)/B_{\text{ref}}$$

$$e_t^* = e_t\big/U_{\text{ref}}^2, \qquad \varepsilon_{e0}^* = \varepsilon_{e0}/\varepsilon_{e0} = 1$$

$$\mu_{e0}^* = \mu_{e0}/\mu_{e0} = 1, \qquad \sigma_e^* = \sigma_e/\sigma_{e\,\text{ref}}$$

$$\mu^* = \mu/\mu_{\text{ref}}, \qquad c_p^* = c_p/c_{p\,\text{ref}}, \qquad k^* = k/k_{\text{ref}}$$

The resulting nondimensional reference parameters are the following:

Reynolds number

$$Re_{\text{ref}} = \frac{\rho_{\text{ref}}U_{\text{ref}}L_{\text{ref}}}{\mu_{\text{ref}}} \tag{20a}$$

Prandtl number

$$Pr_{\text{ref}} = \frac{c_{p\,\text{ref}}\mu_{\text{ref}}}{k_{\text{ref}}} \tag{20b}$$

Mach number

$$M_{\text{ref}} = \frac{U_{\text{ref}}}{\sqrt{\gamma p(\rho_{\text{ref}}, T_{\text{ref}})/\rho_{\text{ref}}}} \tag{20c}$$

Magnetic Reynolds number

$$Re_{m\,\text{ref}} = \sigma_{e\,\text{ref}}\mu_{e0}U_{\text{ref}}L_{\text{ref}} \tag{20d}$$

Magnetic force (or pressure) number

$$R_{b\,\text{ref}} = \frac{B_{\text{ref}}^2}{\rho_{\text{ref}}\mu_{e0}U_{\text{ref}}^2} \tag{20e}$$

In the subsequent sections, the asterisk notation denoting dimensionless variable will be dropped. Thus, all of the equations will be in nondimensional form unless otherwise specified. The MGD equation in physical space is transformed to a computation space and expressed as

$$\frac{\partial \bar{\boldsymbol{Q}}}{\partial t} + \frac{\partial \bar{\boldsymbol{E}}}{\partial \xi} + \frac{\partial \bar{\boldsymbol{F}}}{\partial \eta} + \frac{\partial \bar{\boldsymbol{G}}}{\partial \zeta} + \bar{\boldsymbol{H}} = \frac{\partial \bar{\boldsymbol{E}}_v}{\partial \xi} + \frac{\partial \bar{\boldsymbol{F}}_v}{\partial \eta} + \frac{\partial \bar{\boldsymbol{G}}_v}{\partial \zeta} \tag{21}$$

where

$$\bar{\boldsymbol{Q}} = \frac{\boldsymbol{Q}}{\boldsymbol{J}} \tag{22a}$$

$$\bar{\boldsymbol{E}} = \frac{1}{J}(\xi_x \boldsymbol{E} + \xi_y \boldsymbol{F} + \xi_z \boldsymbol{G}) \tag{22b}$$

$$\bar{\boldsymbol{F}} = \frac{1}{J}(\eta_x \boldsymbol{E} + \eta_y \boldsymbol{F} + \eta_z \boldsymbol{G}) \tag{22c}$$

$$\bar{\boldsymbol{G}} = \frac{1}{J}(\zeta_x \boldsymbol{E} + \zeta_y \boldsymbol{F} + \zeta_z \boldsymbol{G}) \tag{22d}$$

$$\bar{\boldsymbol{H}} = \boldsymbol{H}_M\left(\frac{\partial \bar{B}_x}{\partial \xi} + \frac{\partial \bar{B}_y}{\partial \eta} + \frac{\partial \bar{B}_z}{\partial \zeta}\right) \tag{22e}$$

$$\bar{B}_x = \frac{1}{J}(\xi_x B_x + \xi_y B_y + \xi_z B_z) \tag{22f}$$

$$\bar{B}_y = \frac{1}{J}(\eta_x B_x + \eta_y B_y + \eta_z B_z) \tag{22g}$$

$$\bar{B}_z = \frac{1}{J}(\zeta_x B_x + \zeta_y B_y + \zeta_z B_z) \tag{22h}$$

$$\bar{\boldsymbol{E}}_v = \frac{1}{J}(\xi_x \boldsymbol{E}_v + \xi_y \boldsymbol{F}_v + \xi_z \boldsymbol{G}_v) \tag{22i}$$

$$\bar{\boldsymbol{F}}_v = \frac{1}{J}(\eta_x \boldsymbol{E}_v + \eta_y \boldsymbol{F}_v + \eta_z \boldsymbol{G}_v) \tag{22j}$$

$$\bar{\boldsymbol{G}}_v = \frac{1}{J}(\zeta_x \boldsymbol{E}_v + \zeta_y \boldsymbol{F}_v + \zeta_z \boldsymbol{G}_v) \tag{22k}$$

Expanded expressions of the flux vectors in generalized curvilinear coordinates are provided in Ref. 11.

The convective part of Eq. (21), which attains homogeneity of degree one by introduction of Powell's modification,[7] can be rewritten in terms of flux Jacobian matrices as follows:

$$\frac{\partial \bar{\boldsymbol{Q}}}{\partial t} + \bar{\boldsymbol{A}}\frac{\partial \bar{\boldsymbol{Q}}}{\partial \xi} + \bar{\boldsymbol{B}}\frac{\partial \bar{\boldsymbol{Q}}}{\partial \eta} + \bar{\boldsymbol{C}}\frac{\partial \bar{\boldsymbol{Q}}}{\partial \zeta} = \frac{\partial \bar{\boldsymbol{E}}_v}{\partial \xi} + \frac{\partial \bar{\boldsymbol{F}}_v}{\partial \eta} + \frac{\partial \bar{\boldsymbol{G}}_v}{\partial \zeta} \tag{23}$$

where

$$\bar{\boldsymbol{A}} = \frac{\partial \bar{\boldsymbol{E}}}{\partial \bar{\boldsymbol{Q}}} + \boldsymbol{H}_M \frac{\partial \bar{B}_x}{\partial \bar{\boldsymbol{Q}}} \tag{24a}$$

$$\bar{\boldsymbol{B}} = \frac{\partial \bar{\boldsymbol{F}}}{\partial \bar{\boldsymbol{Q}}} + \boldsymbol{H}_M \frac{\partial \bar{B}_y}{\partial \bar{\boldsymbol{Q}}} \tag{24b}$$

$$\bar{\boldsymbol{C}} = \frac{\partial \bar{\boldsymbol{G}}}{\partial \bar{\boldsymbol{Q}}} + \boldsymbol{H}_M \frac{\partial \bar{B}_z}{\partial \bar{\boldsymbol{Q}}} \tag{24c}$$

Numerical Method

Because of its high-order accuracy and efficiency, the RK4 scheme[12] is used. However, the second-order central differences used in the approximation of the convective terms may produce some spurious numerical oscillations in the region where the convective fluxes dominate and where strong shocks are present. To stabilize the solution, the RK4 scheme is augmented with a TVD model in a postprocessing stage at each iteration level. The TVD model is based on the eigenstructure of the flux Jacobian matrices associated with the convective part of the numerical fluxes. To prevent oscillations, the TVD scheme switches smoothly to first order in the vicinity of a discontinuity, yet changes to second order away from the discontinuity to preserve the order of accuracy of the solution in the smooth regions of the flow.

Eigenvalues and Eigenvectors

The eigenvalues of the flux Jacobian matrix $\bar{\boldsymbol{A}}$ are expressed as

$$\lambda_{0_\xi} = \bar{U} \tag{25a}$$

$$\lambda_{a_{\xi}\pm} = \bar{U} \pm \bar{v}_{a_\xi} \tag{25b}$$

$$\lambda_{f_{\xi}\pm} = \bar{U} \pm \bar{v}_{f_\xi} \tag{25c}$$

$$\lambda_{s_{\xi}\pm} = \bar{U} \pm \bar{v}_{s_\xi} \tag{25d}$$

$$\lambda_{d_\xi} = \bar{U} \tag{25e}$$

where $\bar{U}$, $\bar{v}_{a_\xi}$, $\bar{v}_{f_\xi}$, and $\bar{v}_{s_\xi}$ are the contravariant velocity, Alfvén wave speed, and fast and slow magnetoacoustic wave speeds, respectively. The associated right and left eigenvectors are expressed as

$$\bar{\boldsymbol{R}}_\xi = \begin{bmatrix} \boldsymbol{r}_{0_\xi} & \boldsymbol{r}_{a_{\xi}+} & \boldsymbol{r}_{a_{\xi}-} & \boldsymbol{r}_{f_{\xi}+} & \boldsymbol{r}_{f_{\xi}-} & \boldsymbol{r}_{s_{\xi}+} & \boldsymbol{r}_{s_{\xi}-} & \boldsymbol{r}_{d_\xi} \end{bmatrix} \tag{26a}$$

$$\bar{\boldsymbol{L}}_\xi = \bar{\boldsymbol{R}}_\xi^{-1} = \begin{bmatrix} \boldsymbol{l}_{0_\xi} & \boldsymbol{l}_{a_{\xi}+} & \boldsymbol{l}_{a_{\xi}-} & \boldsymbol{l}_{f_{\xi}+} & \boldsymbol{l}_{f_{\xi}-} & \boldsymbol{l}_{s_{\xi}+} & \boldsymbol{l}_{s_{\xi}-} & \boldsymbol{l}_{d_\xi} \end{bmatrix}^T \tag{26b}$$

Eigenvectors $\bar{\boldsymbol{R}}_\xi$ and $\bar{\boldsymbol{L}}_\xi$ are provided in Ref. 11. The eigenstructure of $\bar{\boldsymbol{B}}$ and $\bar{\boldsymbol{C}}$ are obtained by substituting ξ with η and ζ, respectively.

Modified Runge–Kutta Scheme and TVD Model

The algorithm is expressed as

$$\bar{\boldsymbol{Q}}^{(0)}_{i,j,k} = \bar{\boldsymbol{Q}}^{n}_{i,j,k} \tag{27a}$$

$$\bar{\boldsymbol{Q}}^{(1)}_{i,j,k} = \bar{\boldsymbol{Q}}^{n}_{i,j,k} - \frac{\Delta t}{4}\left(\frac{\partial \bar{\boldsymbol{E}}}{\partial \xi} + \frac{\partial \bar{\boldsymbol{F}}}{\partial \eta} + \frac{\partial \bar{\boldsymbol{G}}}{\partial \zeta} + \bar{\boldsymbol{H}} - \frac{\partial \bar{\boldsymbol{E}}_v}{\partial \xi} - \frac{\partial \bar{\boldsymbol{F}}_v}{\partial \eta} - \frac{\partial \bar{\boldsymbol{G}}_v}{\partial \zeta}\right)^{(0)}_{i,j,k} \tag{27b}$$

$$\bar{\boldsymbol{Q}}^{(2)}_{i,j,k} = \bar{\boldsymbol{Q}}^{n}_{i,j,k} - \frac{\Delta t}{3}\left(\frac{\partial \bar{\boldsymbol{E}}}{\partial \xi} + \frac{\partial \bar{\boldsymbol{F}}}{\partial \eta} + \frac{\partial \bar{\boldsymbol{G}}}{\partial \zeta} + \bar{\boldsymbol{H}} - \frac{\partial \bar{\boldsymbol{E}}_v}{\partial \xi} - \frac{\partial \bar{\boldsymbol{F}}_v}{\partial \eta} - \frac{\partial \bar{\boldsymbol{G}}_v}{\partial \zeta}\right)^{(1)}_{i,j,k} \tag{27c}$$

$$\bar{\boldsymbol{Q}}^{(3)}_{i,j,k} = \bar{\boldsymbol{Q}}^{n}_{i,j,k} - \frac{\Delta t}{2}\left(\frac{\partial \bar{\boldsymbol{E}}}{\partial \xi} + \frac{\partial \bar{\boldsymbol{F}}}{\partial \eta} + \frac{\partial \bar{\boldsymbol{G}}}{\partial \zeta} + \bar{\boldsymbol{H}} - \frac{\partial \bar{\boldsymbol{E}}_v}{\partial \xi} - \frac{\partial \bar{\boldsymbol{F}}_v}{\partial \eta} - \frac{\partial \bar{\boldsymbol{G}}_v}{\partial \zeta}\right)^{(2)}_{i,j,k} \tag{27d}$$

$$\bar{\boldsymbol{Q}}^{(4)}_{i,j,k} = \bar{\boldsymbol{Q}}^{n}_{i,j,k} - \Delta t\left(\frac{\partial \bar{\boldsymbol{E}}}{\partial \xi} + \frac{\partial \bar{\boldsymbol{F}}}{\partial \eta} + \frac{\partial \bar{\boldsymbol{G}}}{\partial \zeta} + \bar{\boldsymbol{H}} - \frac{\partial \bar{\boldsymbol{E}}_v}{\partial \xi} - \frac{\partial \bar{\boldsymbol{F}}_v}{\partial \eta} - \frac{\partial \bar{\boldsymbol{G}}_v}{\partial \zeta}\right)^{(3)}_{i,j,k} \tag{27e}$$

$$\begin{aligned}\bar{\boldsymbol{Q}}^{n+1}_{i,j,k} = \bar{\boldsymbol{Q}}^{(4)}_{i,j,k} &- \frac{1}{2}\frac{\Delta t}{\Delta \xi}\left[(\bar{\boldsymbol{R}}_\xi)^n_{i+\frac{1}{2},j,k}(\bar{\Phi}_\xi)^n_{i+\frac{1}{2},j,k} - (\bar{\boldsymbol{R}}_\xi)^n_{i-\frac{1}{2},j,k}(\bar{\Phi}_\xi)^n_{i-\frac{1}{2},j,k}\right] \\ &- \frac{1}{2}\frac{\Delta t}{\Delta \eta}\left[(\bar{\boldsymbol{R}}_\eta)^n_{i,j+\frac{1}{2},k}(\bar{\Phi}_\eta)^n_{i,j+\frac{1}{2},k} - (\bar{\boldsymbol{R}}_\eta)^n_{i,j-\frac{1}{2},k}(\bar{\Phi}_\eta)^n_{i,j-\frac{1}{2},k}\right] \\ &- \frac{1}{2}\frac{\Delta t}{\Delta \zeta}\left[(\bar{\boldsymbol{R}}_\zeta)^n_{i,j,k+\frac{1}{2}}(\bar{\Phi}_\zeta)^n_{i,j,k+\frac{1}{2}} - (\bar{\boldsymbol{R}}_\zeta)^n_{i,j,k-\frac{1}{2}}(\bar{\Phi}_\zeta)^n_{i,j,k-\frac{1}{2}}\right]\end{aligned} \tag{27f}$$

The convective and diffusion terms are evaluated using second-order central finite differences. The TVD flux limiter function vectors $(\bar{\Phi}_\xi)_{i\pm 1/2,j,k}$, $(\bar{\Phi}_\eta)_{i,j\pm 1/2,k}$, and $(\bar{\Phi}_\zeta)_{i,j,k\pm 1/2}$ for the Davis–Yee symmetric TVD model are provided in Ref. 11.

Validation Cases

To evaluate the performance of the numerical code (RK4TVD), several test cases are considered, for which either analytical solutions or numerical solutions obtained with different methods are available. First, the accuracy and the shock-capturing properties are addressed by solving the MGD shock-tube problem. Second, the implementation of the diffusion terms is validated by simulating Hartmann flow. Finally, the code performance is demonstrated in the computation of multidimensional supersonic flows involving multiple shock waves and expansion waves.

MGD Shock Tube

To validate the shock-capturing properties of the numerical scheme, the MGD shock-tube problem is considered. In this problem, a diaphragm separates a high-pressure region 1 from a low-pressure region 2, as illustrated in Fig. 1. The mesh consists of $801 \times 3 \times 3$ grid points. (For the three-dimensional code, a minimum of three grid points in each direction is required.) Table 1 indicates the initial conditions, as used originally by Brio and Wu[1] and recently by Gaitonde[13] and Canupp.[14] The mesh and the time steps are the same as those employed by Brio and Wu.[1] The tube measures 800 length units with $\Delta x = 1$. The time step is specified as $\Delta t = 0.2$. At $t = 0$, (diaphragm burst) computation starts. Solution is considered after 400 time steps, that is, at $t = 80$.

In Fig. 2, the numerical solution of the RK4TVD scheme is compared to results obtained with two different methods: a fourth-order compact difference scheme (CDS) developed by Gaitonde[13] and a flux vector splitting (FVS) method considered by Canupp.[14] In this numerical simulation, the three different approaches lead to remarkably similar results. For the sake of comparison, the numerical Euler solution computed with the RK4TVD scheme is also provided. In the absence of magnetic field, only three waves are observed, namely, expansion waves propagating to the left, the contact discontinuity, and the normal shock propagating to the right. In the presence of magnetic field, five waves develop, as labeled in Fig. 2a. The five waves are a left-moving fast rarefaction, a slow compound wave, a contact discontinuity, a slow wave, and a right-moving fast rarefaction.

Table 1 MGD shock-tube initial conditions[a]

Region 1	Region 2
$\rho = 1,\ p = 1$	$\rho = \frac{1}{8},\ p = \frac{1}{10}$
$U = \begin{Bmatrix} 0 \\ 0 \\ 0 \end{Bmatrix}, \vec{B} = \begin{Bmatrix} \frac{3}{4} \\ 1 \\ 0 \end{Bmatrix}$	$U = \begin{Bmatrix} 0 \\ 0 \\ 0 \end{Bmatrix}, \vec{B} = \begin{Bmatrix} \frac{3}{4} \\ -1 \\ 0 \end{Bmatrix}$

[a] $\gamma = 2$, $\mu_e = 1$, $\sigma_e \sim +\infty$.

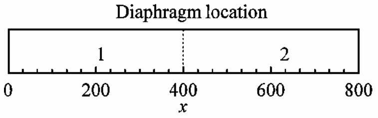

Fig. 1 MGD shock-tube configuration.

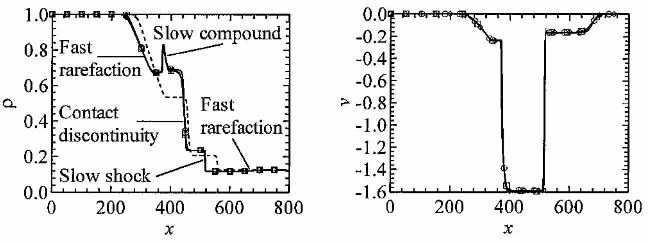

a) Density **d) Velocity *y* component**

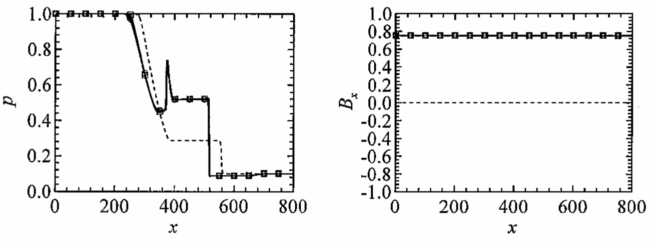

b) Pressure **e) Magnetic field *x* component**

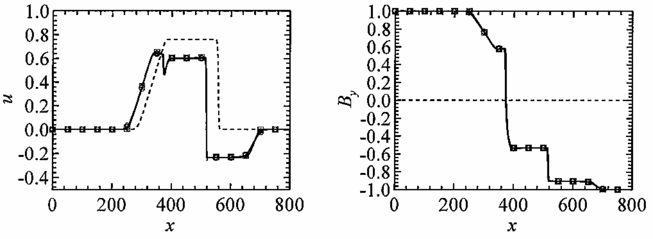

c) Velocity *x* component **f) Magnetic field *y* component**

Fig. 2 MGD shock-tube simulations: ----, without magnetic field; ——, with magnetic field; ○, RK4TVD; □, CDS; and ◇, FVS.

Figure 2a presents the density distribution along the tube. The RK4TVD scheme yields a fractionally higher density on the right side of the slow compound wave, compared to the other schemes. All methods predict nearly identical wave speeds for all of the waves present in the flow. Figure 2b shows the pressure distribution in the tube. Pressure waves are resolved nearly identically by all three methods. The CDS approach produces a slight undershoot in front of the slow shock. Figure 2c illustrates the x component of velocity. The RK4TVD scheme resolves the left-moving fast rarefaction wave slightly better than FVS, but not quite as well as CDS. For the right-moving fast rarefaction wave, CDS yields better resolution, but also produces an undershoot in the velocity on the right side of the slow shock wave. Figure 2d depicts the y component of velocity. All methods yield nearly identical results. In Fig. 2e, it is observed that the x component of magnetic field remains constant throughout the tube, which indicates that the method is divergence free. Figure 2f shows the distribution of the y component of the magnetic field. All methods produce similar solutions.

Both RK4TVD and FVS seem to be more dissipative than CDS. This results in a slight smearing of the waves. However, the artificial viscosity produced by the TVD model in the RK4TVD scheme prevents spurious oscillations such as the undershoot or overshoot observed in the case of the CDS approach.

Hartmann Flow

The nomenclature for the Hartmann problem is provided in Fig. 3. An electrically conducting fluid flows in the x direction between two parallel nonconducting plates. The flow is assumed steady, fully developed, and two dimensional near the centerplane ($w/h \gg 1$). The conducting fluid is incompressible, Newtonian, satisfying the Stokes hypothesis, with uniform viscosity and uniform electrical conductivity. Based on these assumptions, the governing equations (1–10) lead to the following results. $E_y = 0$ and $E_z = E_0$, where E_0 is a constant representing the electric field between the two electrodes, which are connected to either an electric load or a power supply. $B_y = B_0$, where B_0 is a constant representing the applied magnetic field, and $B_z = 0$. The condition under which B_y is not perturbed is that current return paths are provided adjacent to the channel walls. The streamwise pressure gradient $\partial p/\partial x$, which is the pressure head maintaining the flow, is determined to be a constant. The velocity and induced magnetic field distributions, adapted from Ref. 15, can be expressed as follows:

$$u(y) = U_0 Ha_{\text{ref}} \frac{\cosh Ha_{\text{ref}} - \cosh(2y Ha_{\text{ref}}/h)}{Ha_{\text{ref}} \cosh Ha_{\text{ref}} - \sinh Ha_{\text{ref}}} \tag{28}$$

$$B_x(y) = -\mu_{e0} \frac{h}{2} \left(J_0 + \frac{1}{B_0} \frac{\partial p}{\partial x} \right) \frac{\sinh(2y Ha_{\text{ref}}/h)}{\sinh Ha_{\text{ref}}} + \mu_{e0} \frac{1}{B_0} \frac{\partial p}{\partial x} y \tag{29}$$

where

$$U_0 = -\left(\frac{J_0}{\sigma_{e\,\text{ref}} B_0} + \frac{1}{\sigma_{e\,\text{ref}} B_0^2} \frac{\partial p}{\partial x} \right) (Ha_{\text{ref}} \coth Ha_{\text{ref}} - 1) \tag{30}$$

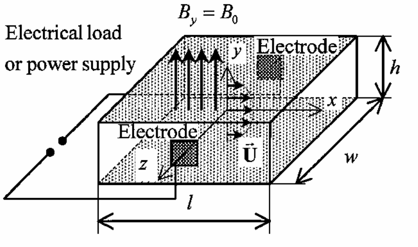

Fig. 3 Schematic of rectangular channel for Hartmann–Poiseuille flow.

U_0 is the mean flow velocity and J_0 is the mean current density across the channel (in the z direction). All parameters in Eqs. (28–30) are provided, except J_0, which can be determined from the following relations:

$$J_0 = -(2/\mu_{e0}h)B_x|_{y=h/2} \tag{31}$$

$$B_x|_{y=h/2} = B_0 Re_{m\,\mathrm{ref}}(K_{\mathrm{ref}} - 1) \tag{32}$$

The similarity parameters of interest are defined as

$$Re_{\mathrm{ref}} = \frac{\rho_{\mathrm{ref}} U_{\mathrm{ref}} L_{\mathrm{ref}}}{\mu_{\mathrm{ref}}}, \qquad Ha_{\mathrm{ref}} = B_0 L_{\mathrm{ref}} \sqrt{\frac{\sigma_{e\,\mathrm{ref}}}{\mu_{\mathrm{ref}}}}$$

$$Re_{m\,\mathrm{ref}} = \sigma_{e\,\mathrm{ref}} \mu_{e0} U_{\mathrm{ref}} L_{\mathrm{ref}}, \qquad K_{\mathrm{ref}} = -\frac{E_0}{U_{\mathrm{ref}} B_0}$$

where

$$L_{\mathrm{ref}} = h/2, \qquad \rho_{\mathrm{ref}} = \rho_\infty, \qquad U_{\mathrm{ref}} = U_0$$

$$\mu_{\mathrm{ref}} = \mu_\infty, \qquad \sigma_{e\,\mathrm{ref}} = \sigma_{e_\infty}$$

For fixed values of Re_{ref}, Ha_{ref}, and K_{ref}, the pressure gradient is specified as

$$\frac{\partial p}{\partial x} = \frac{\rho_{\mathrm{ref}} U_{\mathrm{ref}}^2}{L_{\mathrm{ref}}} \left(K_{\mathrm{ref}} - \frac{Ha_{\mathrm{ref}}}{Ha_{\mathrm{ref}} - \tanh Ha_{\mathrm{ref}}} \right) \frac{Ha_{\mathrm{ref}}^2}{Re_{\mathrm{ref}}} \tag{33}$$

With substitution of Eqs. (31–33), the induced magnetic field can be expressed as

$$B_x(y) = B_0 Re_{m\,\mathrm{ref}} \left[(K_{\mathrm{ref}} - 1)\frac{2y}{h} + \frac{\sinh(2y Ha_{\mathrm{ref}}/h) - (2y/h)\sinh Ha_{\mathrm{ref}}}{Ha_{\mathrm{ref}} \cosh Ha_{\mathrm{ref}} - \sinh Ha_{\mathrm{ref}}} \right] \tag{34}$$

The nondimensional parameter K_{ref} allows the selection of the operating modes, that is, a generator for $0 < K_{\mathrm{ref}} < 1$ and an accelerator for $K_{\mathrm{ref}} > 1$. The case $K_{\mathrm{ref}} = 1$ corresponds to the flow meter because, by measuring E_0 and given B_0, the mean flow velocity U_0 can be determined. For $K_{\mathrm{ref}} = 0$, the channel is short circuited, and all of the current flows in one direction. On the other hand, for $K_{\mathrm{ref}} = 2$, the external power supply forces all of the current to flow in the opposite direction compared to the case $K_{\mathrm{ref}} = 0$.

The boundary conditions (in dimensional form) required for numerical simulations are now described. On the lower and upper sides of the channel, the no-slip velocity condition is enforced and the magnetic field is specified. Parameter K_{ref} is controlled via the value of B_x applied antisymmetrically on the upper and lower sides of the channel. The wall pressure is computed by considering the balance of forces normal to the wall[13] (the y component of momentum equation applied at the wall):

$$\frac{\partial}{\partial y}\left(p_w + \frac{B_{x,w}^2}{2\mu_{e0}} \right) = 0 \tag{35}$$

All primitive variables are extrapolated from the interior domain at the inlet and outlet, except the pressure. Given the inflow static pressure p_0 at midheight ($y = 0$), the distribution of static pressure at the inflow section is calculated using the y component of momentum equation under the assumptions of the Hartmann problem as

$$\forall y \in [-h/2, h/2], \qquad p_i(y) = p_0 - B_x^2(y)\big/2\mu_{e0} \tag{36}$$

At the exit, the static pressure distribution is expressed as

$$\forall y \in [-h/2, h/2], \qquad p_e(y) = p_i(y) + \frac{\partial p}{\partial x} l \tag{37}$$

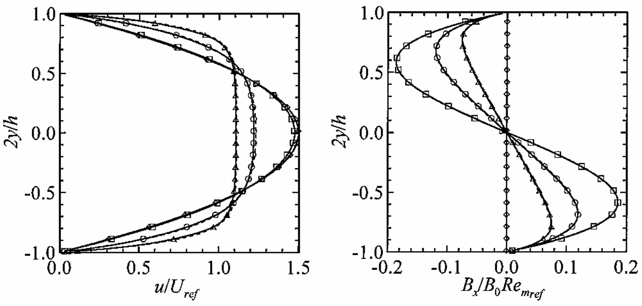

a) Velocity

b) Induced magnetic field

Fig. 4 Poiseuille–Hartmann simulation for various Hartmann numbers: - - - -, analytical solution; ——, numerical solution; ◇, Ha_{ref} = 0; □, Ha_{ref} = 1; ○, Ha_{ref} = 5; and △, Ha_{ref} = 10.

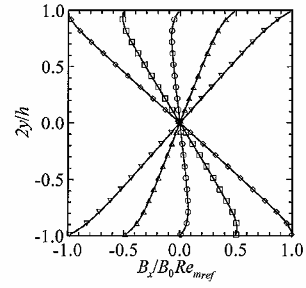

Fig. 5 Poiseuille–Hartmann simulation for various load parameters, induced field B_x: - - - -, analytical solution; ——, numerical solution; ◇, K_{ref} = 0.0; □, K_{ref} = 0.5; ○, K_{ref} = 1.0; △, K_{ref} = 1.5; and ▽, K_{ref} = 2.0.

Numerical simulations are presented for a fixed Reynolds number of $Re_{\mathrm{ref}} = 10^5$ and a fixed magnetic Reynolds number of $Re_{m\,\mathrm{ref}} = 1.83627$. The mean flow Mach number is about 0.086. At such a low Mach number, the numerical solution (which is computed with a compressible flow solver) is unaffected by compressibility and is, thus, consistent with the assumptions of the Hartmann problem. The mesh used consists of $10 \times 101 \times 3$ points. Only a few points in the streamwise direction are necessary because the flow is fully developed. On the other hand, more grid points, with clustering at the wall (minimum spacing $\Delta y/h = 0.00032$), are required in the vertical direction for resolution of the viscous flowfield.

Figure 4 shows the velocity profiles and induced magnetic field at various Hartmann numbers for $K_{\mathrm{ref}} = 1$. The Hartmann number is controlled via the value of B_0 applied symmetrically on the upper and lower sides of the channel. Excellent agreement between numerical and analytical solutions is obtained. At a fixed Reynolds number (i.e., fixed mean flow velocity U_0), the shape of the velocity profile is a function of the Hartmann number only, as expressed by Eq. (28). It is observed that the velocity profiles flatten as the applied magnetic field or Ha_{ref} is increased. To better understand this phenomenon, the expression for Lorentz force is examined: $\boldsymbol{f} = \boldsymbol{J} \times \vec{\boldsymbol{B}}$ with $\boldsymbol{J} = \sigma_{e0}(E_0 + uB_0)\boldsymbol{e}_z$ and $\vec{\boldsymbol{B}} = B_x\boldsymbol{e}_x + B_0\boldsymbol{e}_y$. That is, $\boldsymbol{f} = \sigma_{e0}(E_0 + uB_0)(-B_0\boldsymbol{e}_x + B_x\boldsymbol{e}_y)$. In the case of flow meter ($K_{\mathrm{ref}} = 1$), $E_0 = -U_0B_0$. The channel is open circuited, and the net current flow is zero. Lorentz force is then rewritten as $\boldsymbol{f} = \sigma_{e0}(u - U_0)B_0(-B_0\boldsymbol{e}_x + B_x\boldsymbol{e}_y)$. At the wall, $B_x(\pm h/2) = 0$ and $u(\pm h/2) = 0$. Thus, $\boldsymbol{f} = \sigma_{e0}U_0B_0^2\boldsymbol{e}_x$. Therefore, the force accelerates the flow near the wall. At the centerline, $B_x(0) = 0$ and $u(0) = u_{\max} > U_0$. Thus, the force decelerates the flow at the center of the duct, which explains the flattening of the parabolic profile with increasing applied magnetic field B_0.

The various operating modes are now simulated by varying the parameter K_{ref} for $Ha_{\mathrm{ref}} = 10$ and a fixed Reynolds number. Velocity profiles (not shown) are the same for different values of K_{ref}. However, the induced magnetic field varies with K_{ref} as illustrated in Fig. 5. Numerical simulations and analytical solutions compare very well. The curves $K_{\mathrm{ref}} = 0$ and $K_{\mathrm{ref}} = 0.5$ are similar to the curves $K_{\mathrm{ref}} = 2$ and $K_{\mathrm{ref}} = 1.5$, respectively, except that the magnetic induction lies in the opposite direction, as a result of the current flowing in the opposite direction.

Figure 6 depicts the variation of pressure across the channel for the various values of K_{ref} investigated. Note that the normal pressure gradient at wall is not zero due to the magnetic field applied at the wall.

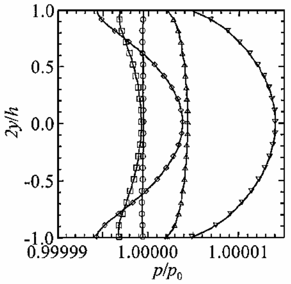

Fig. 6 Poiseuille–Hartmann simulation for various load parameters, pressure profiles: ◇, $K_{ref} = 0.0$; □, $K_{ref} = 0.5$; ○, $K_{ref} = 1.0$; △, $K_{ref} = 1.5$; and ▽, $K_{ref} = 2.0$.

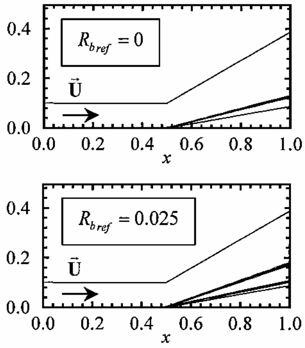

a) Pressure field

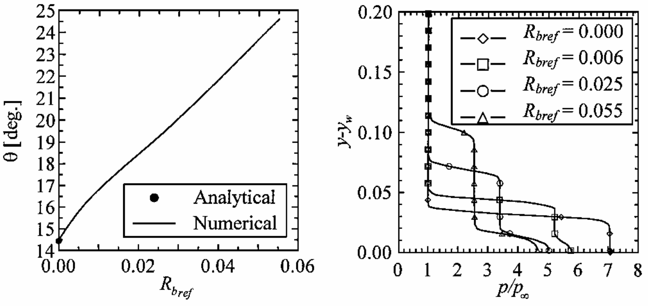

b) Shock-wave angle

c) Pressure profiles at location $x = 0.9$

Fig. 7 Simulation of ideal MGD flow over a 10-deg compression corner.

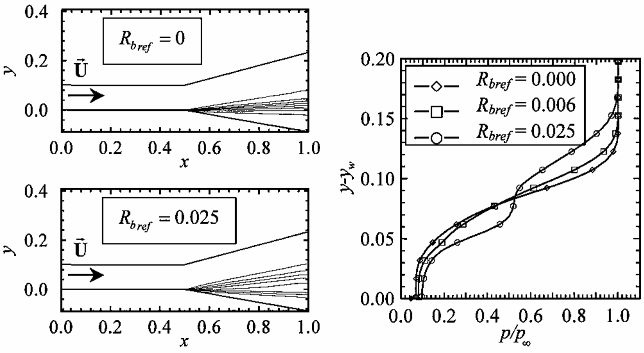

a) Pressure field

b) Pressure profiles at location $x = 0.9$

Fig. 8 Simulation of ideal MGD flow over a 10-deg expansion corner.

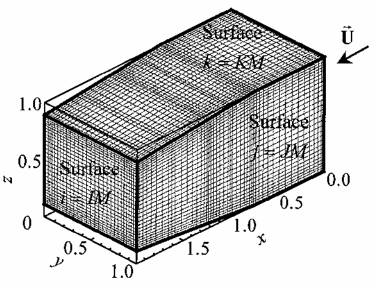

Fig. 9 Mesh, 48 × 31 × 31, for the three-dimensional channel composed of two compression corners.

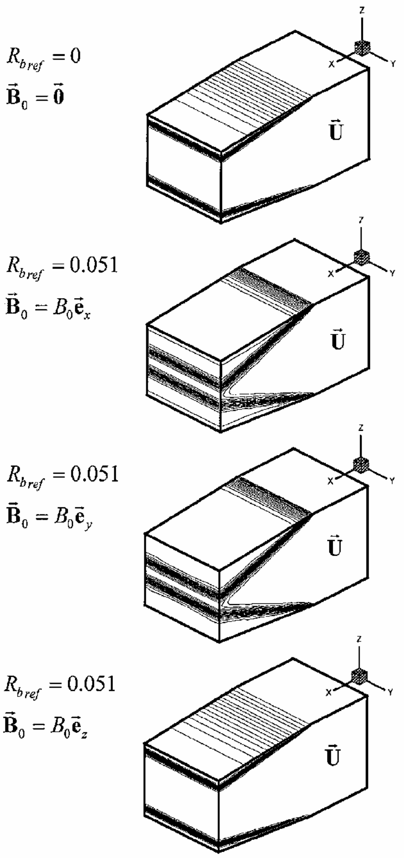

Fig. 10 Simulation of ideal MGD flow in two-dimensional convergent channel; effect of magnetic field orientation on the pressure field.

Supersonic Compression and Expansion Waves

To examine the shock-capturing properties in multidimensional cases, supersonic flows of ideal magnetogas over compression and expansion corners and in convergent channels are addressed. For all of these cases, the boundary conditions are the following. At the inflow, freestream conditions are assumed: $p_\infty = 278.0$ Pa, $T_\infty = 251.0$ K, and $M_\infty = 10.0$, and the magnetic field is applied. At the walls, the slip-velocity condition and zero normal gradients for all properties are imposed. At the outflow and far-field boundaries, zero-order extrapolations are used.

For the supersonic compression and expansion ramps, a mesh consisting of 49 × 41 × 10 grid points is used. The magnetic field is specified as $B_{x0} = B_{y0} = B_{z0} = B_0$. Figure 7 presents the ideal MGD flow simulation over a 10-deg compression corner. The application of magnetic field causes the shock wave angle to increase. Secondary waves develop downstream of the corner near the wall. Examination of the pressure profiles at station $x = 0.9$ length units downstream of the corner shows that the flow undergoes compression across both the shock wave and the secondary waves. Also, the strength of the secondary wave increases with the magnetic field, whereas the strength of the external shock wave reduces and wall pressure (at location $y = y_w$) drops with the magnetic field. Figure 8 depicts the ideal MGD flow simulation over a 10-deg expansion corner. In the presence of a magnetic field, the expansion fan angle increases and new waves develop in the flow.

The effect of the orientation of magnetic field is investigated by considering a converging channel along the x axis, as illustrated in Fig. 9. The walls at $k = 1$ and $k = KM$ consist of 5-deg compression corners and the walls at $j = 1$ and $j = JM$ are flat. As shown in Fig. 10, the application of magnetic field in the x direction or in the y direction produces a significant increase in the shock wave angle. On the other hand, application of magnetic field in the z direction leads to no significant effect, compared to the Euler solution.

Now, to demonstrate the performance of the algorithm in the computation of three-dimensional flows, a shock/shock interaction problem is solved in a convergent channel, as illustrated in Fig. 11. The

Fig. 11 Mesh, 48 × 31 × 31, for the three-dimensional channel composed of three compression corners.

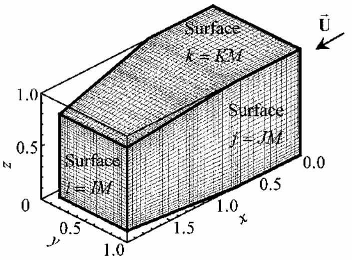

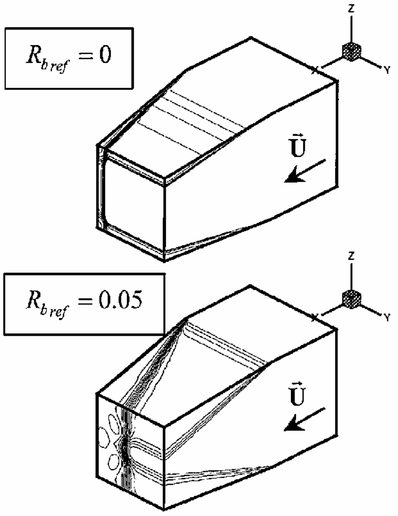

Fig. 12 Simulation of ideal MGD flow in three-dimensional convergent channel, effect of magnetic field on the pressure field.

walls at $k = 1$ and $k = KM$ consist of 5-deg compression corners, the wall at $j = 1$ is a 10-deg compression corner and the wall at $j = JM$ is a plane. A longitudinal magnetic field is applied, $B_{x0} = B_0$ and $B_{y0} = B_{z0} = 0$.

Numerical simulations are conducted for a longitudinal magnetic field $(B_{x0}, B_{y0}, B_{z0}) = (B_0, 0, 0)$. Figure 12 presents the magnetic effect on the pressure field. In the absence of a magnetic field, shock waves interfere at the edges. In the presence of a magnetic field, the shock wave angles increase, as expected.

Conclusions

A computer code utilizing an RK4 scheme augmented with the Davis–Yee symmetric TVD model has been developed to solve MGD equations in three dimensions. The algorithm is designed for simulation of steady or unsteady, compressible, inviscid, or viscous flows.

The method has been validated by solving various benchmark problems. The first test case was the one-dimensional MGD shock-tube problem validating the TVD model. Excellent agreement with the existing numerical solutions has been obtained. The Hartmann problem has been solved to verify the addition of the viscous and resistive terms. For the range of Hartmann numbers investigated, numerical and analytical solutions have compared very well. Finally, high-speed supersonic flows involving compression and expansions waves have been computed to demonstrate the shock-capturing capability of the scheme in multiple dimensions.

Acknowledgments

This work was sponsored by the Air Force Office of Scientific Research, U.S. Air Force, under tasks monitored by S. Walker and J. Schmisseur. The authors acknowledge the support of Kansas National Science Foundation Cooperative Agreement EPS-9874732 and the Wichita State University High Performance Computing Center. The authors also thank D. V. Gaitonde and P. W. Canupp for providing data from their magnetogasdynamic shock-tube simulation for comparison purposes and J. Shang for several useful conversations.

References

[1] Brio, M., and Wu, C. C., "An Upwind Differencing Scheme for the Equations of Ideal Magnetohydrodynamics," *Journal of Computational Physics*, Vol. 75, 1988, pp. 400–422.

[2] Zachary, A. L., and Colella, P., "A Higher-Order Godunov Method for the Equations of Ideal Magnetohydrodynamics," *Journal of Computational Physics*, Vol. 99, 1992, pp. 341–347.

[3] Dai, W., and Woodward, P. R., "An Approximate Riemann Solver in Magnetohydrodynamics," Univ. of Minnesota Supercomputer Inst., Research Rept. UMSI 91/329, Minneapolis, MN, Dec. 1991.

[4] Dai, W., and Woodward, P. R., "A Simple Riemann Solver and High-Order Godunov Schemes for Hyperbolic Systems of Conservation Laws," *Journal of Computational Physics*, Vol. 121, 1995, pp. 51–65.

[5] Harada, S., Augustinus, J., Hoffmann, K. A., and Agarwal, R. K., "Development of a Modified Runge–Kutta Scheme with Total Variation Diminishing Limiters for the Ideal One-Dimensional Magnetogasdynamic Equations," AIAA Paper 97-2090, June–July 1997.

[6] Augustinus, J., Harada, S., Hoffmann, K. A., and Agarwal, R. K., "Numerical Solution of the Modified Eight-Wave Structure Ideal Magnetogasdynamic Equations by Modified Runge–Kutta Scheme with Total Variation Diminishing," AIAA Paper 97-2398, June 1997.

[7] Powell, K. G., "An Approximate Riemann Solver for Magnetohydrodynamics (that Works in More than One Dimension)," NASA CR 194902, Inst. for Computer Applications in Science and Engineering, Rept. 94-24, Hampton, VA, April 1994.

[8] Augustinus, J., Hoffmann, K. A., and Harada, S., "Effect of Magnetic Field on the Structure of High-Speed Flows," *Journal of Spacecraft and Rockets*, Vol. 35, No. 5, 1998, pp. 639–646.

[9] Harada, S., Hoffmann, K. A., and Augustinus, J., "Development of a Modified Runge–Kutta Scheme with Total Variation Diminishing Limiters for the Ideal Two-Dimensional Magnetogasdynamic Equations," AIAA Paper 98-0981, Jan. 1998.

[10] Damevin, H. M., Dietiker, J. F., and Hoffmann, K. A., "Hypersonic Flow Computations with Magnetic Field," AIAA Paper 2000-0451, Jan. 2000.

[11] Damevin, H. M., "Development of Numerical Techniques for Simulation of Magnetogasdynamics and Hypersonic Chemistry," Ph.D. Dissertation, Dept. of Aerospace Engineering, Wichita State Univ., Wichita, KS, Dec. 2001.

[12] Jameson, A., Schmidt, W., and Turkel, E., "Numerical Solution of the Euler Equations by Finite Volume Methods Using Runge–Kutta Time-Stepping Schemes," AIAA Paper 81-1259, June 1981.

[13] Gaitonde, D. V., "Development of a Solver for Three-Dimensional Non-ideal Magnetogasdynamics," AIAA Paper 99-3610, June 1999.

[14] Canupp, P. W., "Resolution of Magnetogasdynamic Phenomena Using a Flux-Vector Splitting Method," AIAA Paper 2000-2477, June 2000.

[15] Boyd, T. J. M., and Sanderson, J. J., *Plasma Dynamics*, Barnes and Noble, New York, 1969.

I. D. Boyd
Associate Editor